Spectroelectrochemical Behavior of Cr, Fe, Co, and Ni in LiCl-KCl Molten Salt for Decontaminating Radioactive Metallic Wastes

Journal of The Electrochemical Society, 2021 **168** 013504

Spectroelectrochemical Behavior of Cr, Fe, Co, and Ni in LiCl-KCl Molten Salt for Decontaminating Radioactive Metallic Wastes

Seokjoo Yoon and Sungyeol Choi[z]

Department of Nuclear and Quantum Engineering, Korea Advanced Institute of Science and Technology, Daejeon 34141, Republic of Korea

This study examines the thermodynamic, kinetic, and spectroscopic behaviors of Cr, Fe, Co, and Ni to lay the foundation to develop an electrochemical decontamination process for radioactive metallic wastes. Cyclic voltammetry combined with numerical fitting was used to obtain the formal potentials, standard rate constants, and diffusion coefficients of redox reactions, Cr(II)/Cr, Fe(II)/Fe(0), Co(II)/Co(0), and Ni(II)/Ni(0), in LiCl-KCl at 773 K. The order of the diffusion coefficients was 10^{-5} cm^2 s^{-1}, which agrees with the existing data and the standard rate constants showed similar values with the order of 10^{-3} cm s^{-1} between experimental correlations and numerical fitting. UV–vis-NIR absorption spectroscopy of the metallic constituents was performed to derive molar absorption coefficients and molecular structures in molten salt media. In particular, the redox reaction of Cr(III)/Cr(II) was investigated by chronoabsorptometry to obtain its formal potential, the number of electrons, and the diffusion coefficient of Cr(II). The obtained reaction properties were used in the numerical modeling of the ECE reaction in a Ni and Co binary system to reproduce the experimental results of CV, revealing the presence of chemical reaction. The findings of this study will be directly used for designing a decontamination process to produce acceptable waste forms and reduce waste volume.

 [DOI: 10.1149/1945-7111/abdc7e]

Manuscript submitted November 16, 2020; revised manuscript received January 5, 2021. Published January 29, 2021.

Supplementary material for this article is available online

Radioactive metallic waste produced from nuclear power plants commonly contains Cr, Fe, and Ni as alloying constituents and Co as an impurity.[1,2] Structural components containing these metallic elements are activated in volume or contaminated on surfaces. In particular, radioactive isotopes are distributed in the volume of the reactor internals and pressure vessels made of steel alloys because of neutron activation reactions. Such radioactive waste must be decontaminated to reduce the volume of final waste as well as to meet the waste acceptance criteria of the final repository.[3] In addition, decontaminating the waste can change waste categories from intermediate level waste to low level waste.[4,5]

An electrorefining process using molten salt has been developed to treat and recycle nuclear materials in used nuclear fuel.[6–11] The concept underlying the process can also be used as a decontamination option when radioactive contaminants exist at levels deeper than the surface oxide layers.[3,5] This process was originally developed for recovering uranium from used nuclear fuel. During electrorefining, the contaminated structural components are dissolved into a lithium chloride-potassium chloride (LiCl-KCl) electrolyte. The electrode potential is controlled to selectively recover each component by depositing it on the surfaces of a metallic cathode.[12–14] Therefore, the thermodynamic, kinetic, and spectroscopic behavior of reduction-oxidation reactions is significant to design and optimize the decontamination process.

Some researchers have attempted to apply electrochemical methods for the metallic constituents of nuclear power plant components in LiCl-KCl.[15–20] In 2017, Park et al., examined redox behaviors of Zr, Sn, Cr, Fe, and Co in LiCl-KCl using W working electrodes to develop a Zircaloy-4 decontamination process.[15] In 2020, Choi et al. investigated the possibility of separating Ni and Co in LiCl-KCl using chronopotentiometry (CA) and cyclic voltammetry (CV).[21] However, few studies have explored electrochemical redox reactions at high temperature molten salts while simultaneously monitoring changes in oxidation state using absorption spectroscopy. The spectroelectrochemical measurements were performed only for some elements such as Eu,[22] Sm,[23] and U.[24] The rate constants of redox reactions were rarely obtained. For this reason, the reversibility of the electrochemical systems according to the scan rates of CV has often been ignored. Moreover, the obtained properties have not been applied to explain observed experimental phenomena to show their applicability and completeness.

In this study, CV was used to characterize redox reactions of Fe(II)/Fe(0), Ni(II)/Ni(0), Co(II)/Co(0), Cr(II)/Cr(0), and Cr(III)/Cr(II). The formal potentials and standard rate constants of the redox reactions were measured by CV results from both correlations and numerical fitting. The diffusion coefficients were obtained and compared in terms of both CV and CA results. The molar absorption coefficients and molecular structures of the ions were obtained by UV–vis-NIR absorption spectroscopy (250–950 nm). In particular, the redox reaction of Cr(III)/Cr(II) was investigated by combining spectroscopy and electrochemistry in the same unit cell to obtain its formal potential, the number of electrons, and the diffusion coefficient of Cr(II). As a case example, the electrochemical-chemical-electrochemical (ECE) reaction mechanisms of a recently reported[21] Ni and Co binary system were successfully explained by numerical modeling combined with the obtained reaction properties.

Experimental

Preparation of molten salts.—All storages, preparations, and experiments using all chemicals and electrolytes were performed under an Ar atmosphere. A mixture of eutectic LiCl(44 wt%)–KCl (56 wt%) (99.9%, anhydrous, Alfa Aesar) was first dried at 473 K for 6 h to remove all possible excess moisture in the salt, and then the molten salt was melted in a quartz cell inside an electric furnace. We used iron(II) chloride ($FeCl_2$, 99.9%, anhydrous, Sigma Aldrich), nickel(II) chloride ($NiCl_2$, 99.99%, anhydrous, Sigma Aldrich), cobalt (II) chloride ($CoCl_2$, 99.9%, anhydrous, Alfa Aesar), chromium(II) chloride ($CrCl_2$, 99.9%, anhydrous, Alfa Aesar), and chromium(III) chloride ($CrCl_3$, 99.9%, anhydrous, Alfa Aesar). Each transition metal chloride salt was mixed with LiCl-KCl up to 5 wt%, and the mixture was pre-melted at 773 K for 12 h. A mixture of 0.5 wt% of transition metal chloride in LiCl-KCl was then prepared by mixing the pre-melted salts and the LiCl-KCl eutectic. 1 wt% of silver(I) chloride (AgCl, 99.99%, anhydrous, Sigma Aldrich) was added to LiCl-KCl as an electrolyte for a reference electrode.

Preparation of electrochemical cells and electrodes.—Figure 1 shows a schematic diagram of an electrochemical cell. The electrochemical cell was configured with a closed-end round tip quartz cell (ID: 15 mm, OD: 25 mm, length: 350 mm). For performing

[z]E-mail: sungyeolchoi@kaist.ac.kr

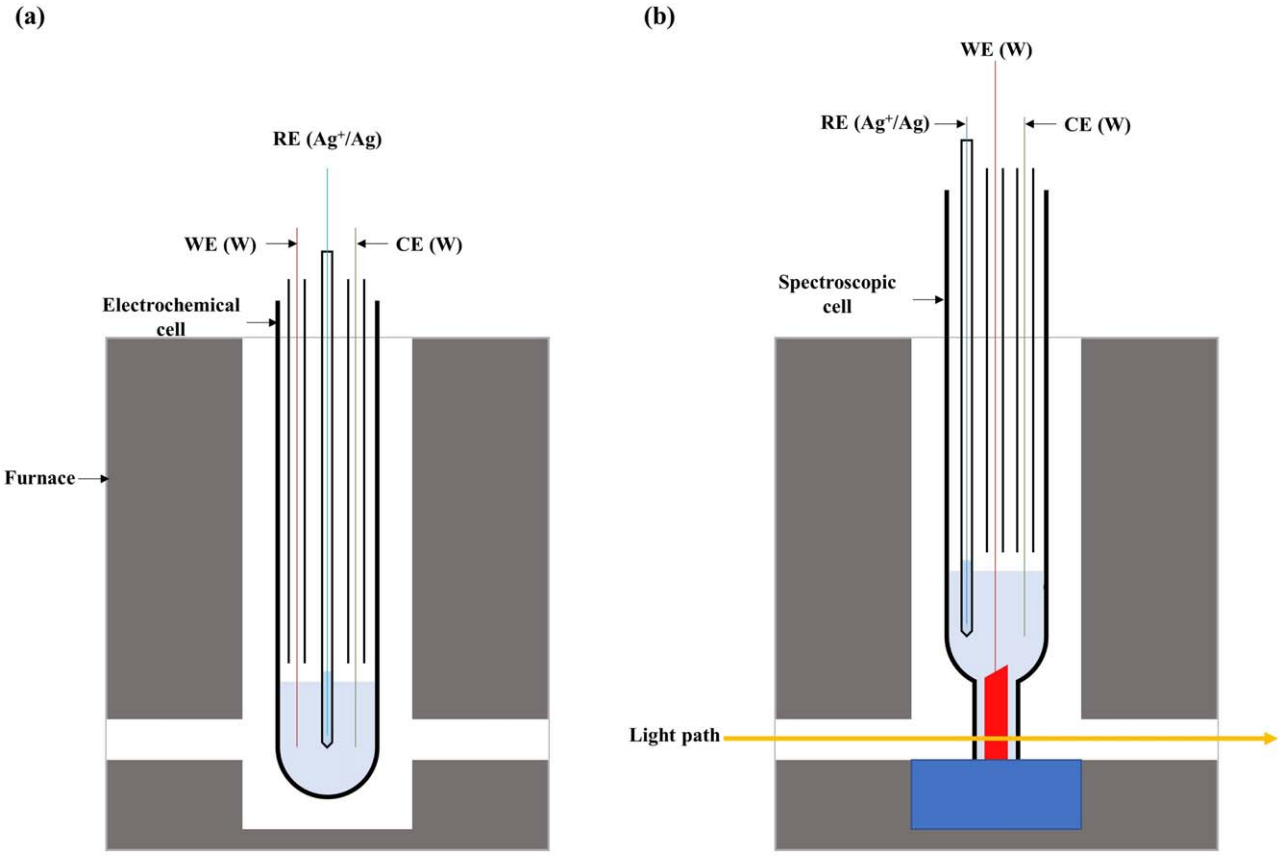

Figure 1. Schematics of (a) system for electrochemistry and (b) system for spectroscopy and spectroelectrochemistry.

spectroelectrochemistry, a quartz tube (ID: 25 mm, OD: 35 mm) was connected to a square quartz cuvette (light path length: 10 mm) at the bottom of the cell. All quartz containers were washed in an ultrasonic washing machine with DI water, rinsed in acetone, and then dried in a vacuum oven for more than 12 h. The operating temperature of the cell was measured by inserting a K-type thermocouple covered with a quartz tube into molten salt.

A 3-electrode system was used to measure electrochemical behaviors in the cell. The working and counter electrodes were tungsten (W) wires (99.95%, Alfa Aesar) with a diameter of 1.25 mm for electrochemical measurements. The surface area of the working electrode was determined by measuring the immersed depth of the working electrode using a digital caliper. The working electrode was changed to a W mesh (99.9%, 20-mesh, Alfa Aesar) connected to a W wire (99.95%, Alfa Aesar) for spectroelectrochemical measurements. To prevent contact between these electrodes, they were partially sheathed with a quartz tube positioned slightly above the level of the molten salt. For the Ag^+/Ag reference electrode, a 1 mm diameter silver wire (99.99%, Alfa Aesar) was inserted into a mixture of LiCl–KCl–AgCl(1 wt%) within a thin-walled Pyrex tube of 4 mm OD × 2 mm ID × 350 mm, as done in the previous research by authors.[25] All of the metallic electrodes were polished with 600-grit silicon carbide paper and washed with ultrapure water for 1 h in an ultrasonic bath. This procedure was repeated with 1200-grit silicon carbide paper, and the electrodes were dried in a vacuum oven (100 °C) for at least 12 h.

Electrochemistry and absorption spectroscopy apparatus.—A glove box was used for all experiments to maintain an inert Ar atmosphere. The concentration of oxygen and moisture was kept at about 1 ppm. At the bottom of the glove box, a high temperature electric furnace is equipped with a programmable temperature controller. All electrochemical tests were performed in the electric furnace using a ceramic heater. Quartz windows were attached at the bottom of the furnace to make a light path for spectroscopic measurements. Water cooling was applied to the interface between the electric furnace and the bottom of the glove box to prevent thermal damage to the glove box and reduce its temperature. All electrochemical measurements, CV and CA, were performed using a PARSTAT 4000A potentiostat/galvanostat (Princeton Applied Research). Low resistance BNC cables connected the instrument to the electrochemical cell through the glovebox. UV–vis-NIR absorption spectroscopy was performed using an MCS 601 spectrometer (ZEISS) combined with a CLH-600 halogen lamp (320-2400 nm, ZEISS) and a CLD-600 deuterium lamp (215-640 nm, ZEISS), and spectra were measured from 250 to 950 nm.

Numerical fitting and modeling.—Numerical fitting of cyclic voltammograms was performed using a Digielch 8 program (ElchSoft). Fitted parameters to reconstruct CV curves in the software are formal potentials, diffusion coefficients, and reaction rate constants. The simulation of the cyclic voltammogram adopts the adaptive finite element method (AFEM) to explain the electrochemical diffusion-kinetics and adsorption phenomena developed by Rudolph.[26] The parameters were fitted by the non-linear regression method where the standard deviation between simulated and experimental data is minimized. The optimization of the curve is achieved by the iterative Gauss-Newton method.

For the initial guess of the parameters, the correlations widely used for the analysis of cyclic voltammograms are utilized. The charge transfer coefficient was assumed to be 0.5 in the redox reactions. The correlations for the driving formal potentials, diffusion coefficients, and standard rate constants are given in Eqs. 1–7. All are valid for quasi-reversible reactions, and the values obtained from the following correlations are compared to those obtained from simulated voltammograms.

The formal potential can be calculated from the CV results with the following equation for soluble-insoluble redox pairs:[27]

$$E^{0'} = E_p - \frac{RT}{nF}\ln(C_{M^{n+}}) - 0.8540\frac{RT}{nF} + E_{Ag+/Ag}, \quad [1]$$

where $E^{0'}$ is the formal potential, E_p is the peak reduction potential, R is the universal gas constant, T is the absolute temperature, n is the number of electrons involved in the electrochemical reaction, F is the Faraday constant, and $C_{M^{n+}}$ is the initial molar concentration of metal species. .. is the electrode potential of the Ag^+/Ag reference electrode, and it can be derived using the following formula:[15,28]

$$E_{Ag+/Ag} = E^0_{Ag+/Ag} + \frac{RT}{F}\ln(C_{Ag^+}) \quad [2]$$

where $E^0_{Ag+/Ag}$ is the standard electrode potential of Ag+/Ag electrode reaction, and C_{Ag^+} is the molar concentration of Ag^+. The $E^0_{Ag+/Ag}$ at 773 K has been suggested by various research groups, as shown in Table I.[29–32] $E^0_{Ag+/Ag}$ suggested by Shirai et al. shows higher values compared to the other three values, which may be due to the different dissolution kinetics of Ag^+ in the reference electrode.[33] Depending on which $E^0_{Ag+/Ag}$ values to choose, the formal potential value can be changed. In this study, $E^0_{Ag+/Ag}$ suggested by Yang and Hudson was chosen, since this value is close to the values suggested by Yoon et al. and Barin et al. The $E_{Ag+/Ag}$ value calculated from this formula is −1.045 V vs Cl_2/Cl^-.

The diffusion coefficient can be calculated from the CV results with the Berzins-Delahay equation for soluble-insoluble redox pairs:[34]

$$i_p = 1.082nFAC_{M^{n+}}\sqrt{\frac{nFDv}{RT\pi}} \quad [3]$$

where i_p is the peak reduction current, A is the electrode surface area, D is the diffusion coefficient, and v is the scan rate.

The diffusion coefficient can be calculated from the CA results with the Cottrell equation:[35]

$$i = nFAC\sqrt{\frac{D}{\pi t}} \quad [4]$$

where i is the current and t is time.

The standard rate constant can be calculated from the CV results with the Nicholson relationship:[36]

$$\psi_{298} = \frac{-0.6288 + 0.0021X}{1 - 0.017X} = \frac{k^0}{\sqrt{\frac{\pi DnFv}{298R}}},$$
$$X = n * \Delta E_{p-p,298K} \quad [5]$$

where ψ_{298} is a unitless parameter to determine the standard rate constant at 298 K, k^0 is the standard rate constant, and $\Delta E_{p-p,298K}$ is the difference between the anodic and cathodic peak potentials. ΔE_{p-p} and ψ at 773 K are transformed to their corresponding values at 298 K by the following formula:

$$\Delta E_{p-p,298} = \frac{\Delta E_{p-p,T} * 298}{T}, \ \psi_T = \psi_{298}\sqrt{\frac{T}{298}} \quad [6]$$

where $\Delta E_{p-p,T}$ is the peak-to-peak potential at a given temperature and ψ_T is a unitless parameter to determine standard rate constants at a given temperature.

The reversibility factor can be calculated by Λ suggested by Matsuda and Ayabe:[37]

$$\Lambda = \frac{k^0}{\sqrt{\frac{nFDv}{RT}}} \quad [7]$$

where Λ is the reversibility factor. The criteria for determining the electrochemical reversibility are given as follows:

$\Lambda \geqslant 15$ or $k^0 \geqslant 0.3v^{0.5}$: electrochemically reversible reaction.

$15 > \Lambda \geqslant 10^{-3}$ or $0.3v^{0.5} > k^0 \geqslant 2{\cdot}10^{-5}\,v^{0.5}$: electrochemically quasi-reversible reaction.

$\Lambda < 10^{-3}$ or $k^0 < 2{\cdot}10^{-5}\,v^{0.5}$: electrochemically irreversible reaction.

Results and Discussion

Thermodynamics of Cr(II)/Cr(0), Fe(II)/Fe(0), Co(II)/Co(0), Ni(II)/Ni(0).—The electrochemical reactions of Cr(II), Fe(II), Co(II), and Ni(II) ions dissolved in LiCl-KCl were investigated on a W working electrode at 773 K. The experimental conditions for the electrochemical measurements are summarized in Table II. Figure 2 shows cyclic voltammograms of the metallic ions. The higher anodic peak compared to the cathodic peak in the voltammograms indicates the presence of adsorption kinetics. The scan rate varies over at least 30 times from 0.05 to 1.5 V s^{-1} to verify the reaction mechanisms.[38] The scan starts from the positive potential to the negative potential and returns to the original potential. The observed redox peaks of Cr (II), Fe(II), Co(II), and Ni(II) in LiCl-KCl were consistent with the previous measurements obtained by Park et al., 2017 and Iizuka et al., 2001.[15,16] All four ions showed single step reduction reactions to metallic forms of Cr, Fe, Co, and Ni, as expressed in Eqs. 8–11.

$$Cr^{2+} + 2e^- \rightleftarrows Cr \quad [8]$$

$$Fe^{2+} + 2e^- \rightleftarrows Fe \quad [9]$$

$$Co^{2+} + 2e^- \rightleftarrows Co \quad [10]$$

$$Ni^{2+} + 2e^- \rightleftarrows Ni \quad [11]$$

Table I. $E^0_{Ag+/Ag}$ value suggested by different research groups.

	Yang and Hudson[29]	Yoon et al.[30]	Shirai et al.[31]	Barin et al.[32]
$E^0_{Ag+/Ag}$ (vs Cl_2/Cl^-)	−0.9004	−0.8973	−0.8125	−0.9245

Table II. Summary of experiment conditions for electrochemical measurements.

Electrode reaction	Concentration (M)	Surface area of the electrode (cm^2)	Scan range for CV (V vs Ag^+/Ag)	Applied potential for CA (V vs Ag^+/Ag)
Cr(II)/Cr	0.0683	1.06	−1.0–0.0	−0.9
Fe(II)/Fe	0.0662	1.02	−0.6–0.4	−0.6
Co(II)/Co	0.0625	0.511	−0.5–0.3	−0.4
Ni(II)/Ni	0.0627	1.02	−0.5–0.5	−0.2

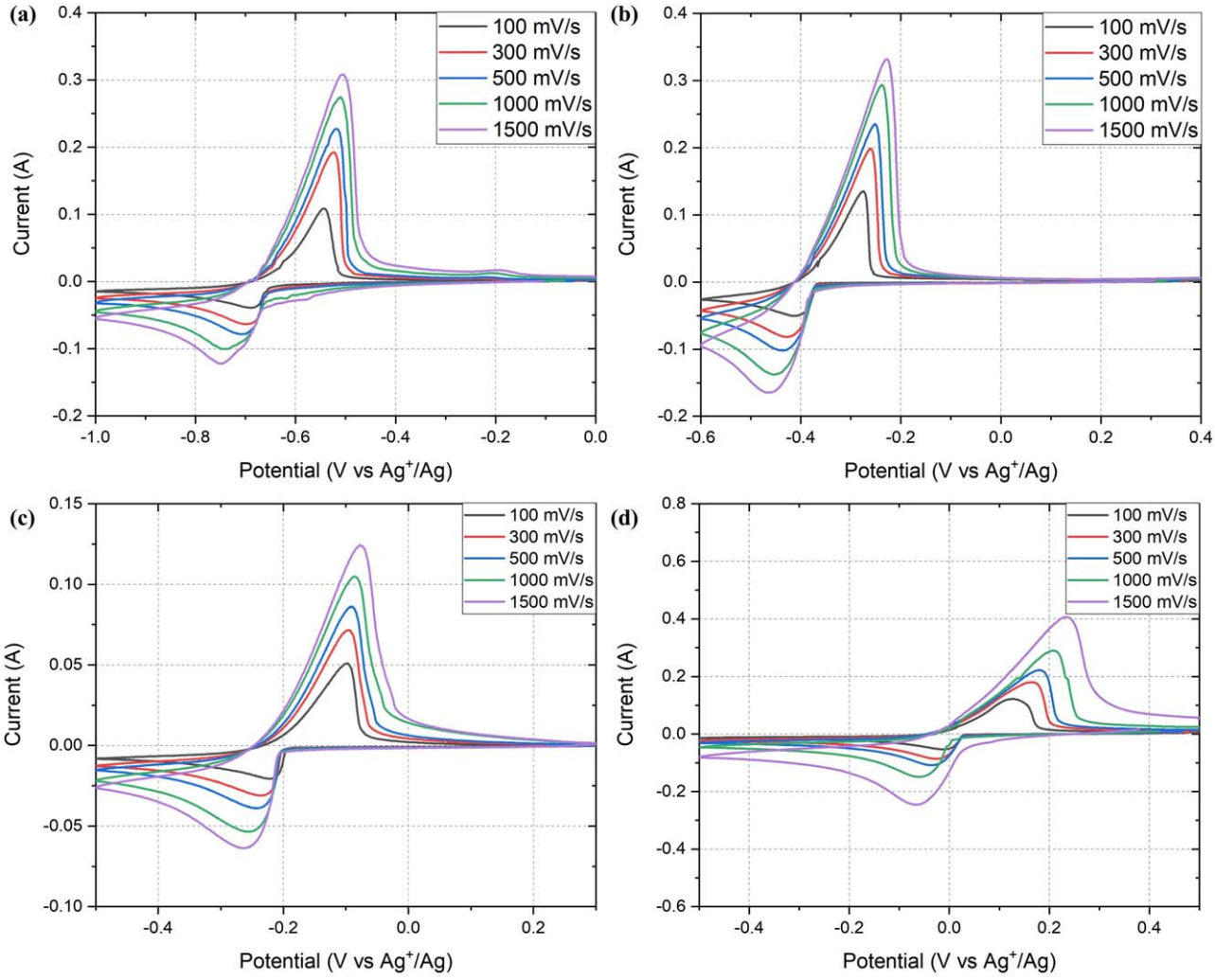

Figure 2. Cyclic voltammograms of (a) Cr(II)/Cr(0), (b) Fe(II)/Fe(0), (c) Co(II)/Co(0), and (d)Ni(II)/Ni(0) in LiCl-KCl eutectic at 773 K. WE: Tungsten 1.25 mm diameter; CE: Tungsten 1.25 mm diameter; RE: Ag/Ag^{+} (1 wt% AgCl in LiCl-KCl), (a): [Cr(II)] = 0.0683 mol l^{-1} and A = 1.06 cm^2, (b): [Fe(II)] = 0.0662 mol l^{-1} and A = 1.02 cm^2, (c): [Co(II)] = 0.0625 mol l^{-1}, A^{-1} = 0.511 cm^2, (d): [Ni(II)] = 0.0627 mol l^{-1} and A = 1.02 cm^2.

Figure 3 shows the formal potentials of the four reactions. The results of numerical fitting and correlations were compared with previously reported values (see Table SI (available online at stacks.iop.org/JES/168/013504/mmedia)). All formal potentials are in acceptable ranges with no changes of the relative redox reaction trends. Ni(II) is reduced to Ni(0) at the most positive potential, while Cr(II) is reduced to Cr(0) at the most negative potential. Thus, LiCl–KCl–$NiCl_2$ would be the initial molten salt composition to prevent undesirable Co deposition.

For the simulation of the cyclic voltammograms of Cr, Fe, Co, and Ni, the charge transfer reaction of $M^{2+} + 2e^{-} = M$ is adopted to Digielch8 with the adsorption. The charge transfer coefficient is assumed as 0.5. Modeling parameters for the adsorption phenomena were obtained from Fabian et al., 2012[39] where the metallic species are adsorbed to the electrode while the ionic species are not. The equilibrium constant K^{*}, adsorption rate constant k_f^{*}, and the Frumkin isotherm factor a* for $M^{2+*} = M^{2+}$ at 773 K are given as 1×10^{-10}, 1×10^{-6}, and -2.5, respectively, for all four elements. Similarly, K*, kf*, and a* for $M^{*} = M$ are given as 3, 1×10^{5}, and 2.85, respectively. The maximum surface coverage (mol/cm^2) is given as $1 * 10^{-6}$. Using these parameters, the cyclic voltammograms of Cr, Fe, Co, and Ni are simulated and the formal potential, standard rate constants, and diffusion coefficients are numerically fitted from the voltammograms.

The experimental data and simulated results are compared in Figure 4. The anodic peaks are well-matched, while the cathodic

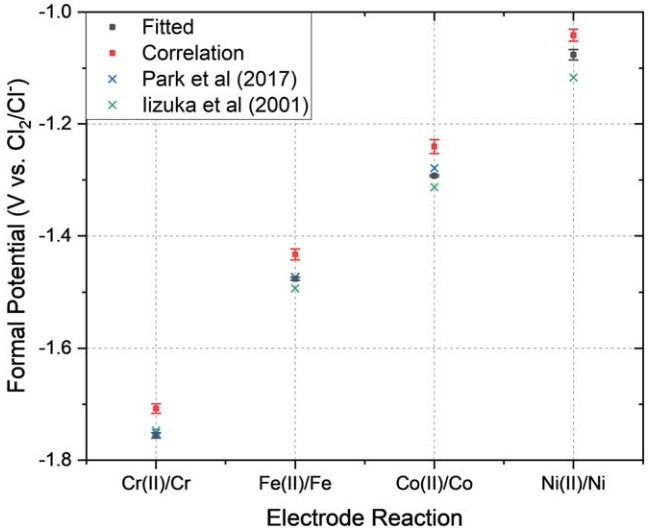

Figure 3. Formal potentials of four electrode reactions: Cr(II)/Cr, Fe(II)/Fe, Co(II)/Co(0), Ni(II)/Ni(0).

peaks show some deviations. This occurs due to the nucleation and growth mechanism not being implemented in the software.[39,40] Interactions between the metal and substrate and how the metal is

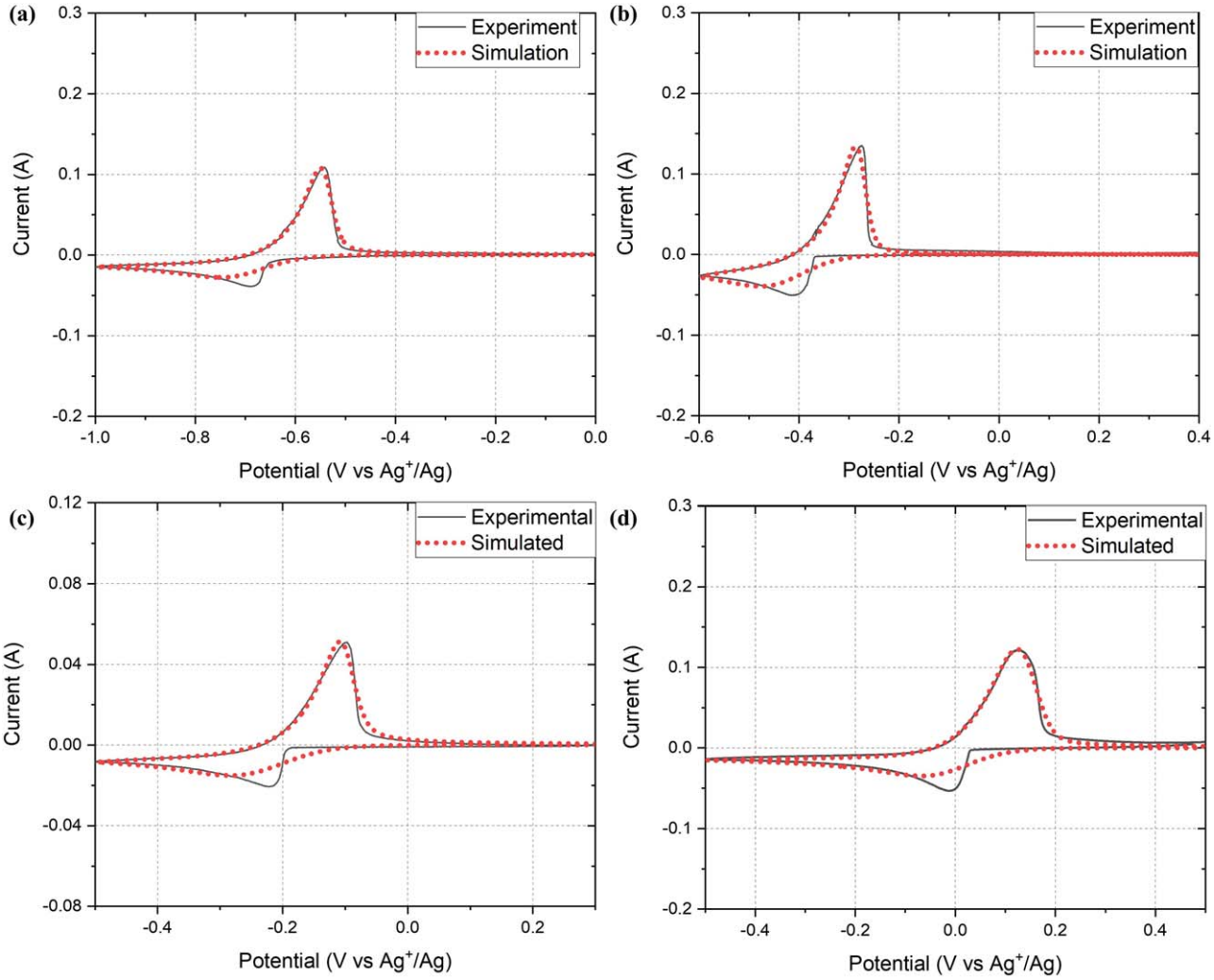

Figure 4. Comparison of experimental data and simulated data for cyclic voltammetry of (a) Cr(II)/Cr, (b) Fe(II)/Fe, (c) Co(II)/Co, and (d) Ni(II)/Ni. WE: Tungsten 1.25 mm diameter; CE: Tungsten 1.25 mm diameter; RE: Ag/Ag^+ (1 wt% AgCl in LiCl-KCl), (a): [Cr(II)] = 0.0683 mol l^{-1} and A = 1.06 cm^2, (b): [Fe(II)] = 0.0662 mol l^{-1} and A = 1.02 cm^2, (c): [Co(II)] = 0.0625 mol l^{-1}, A = 0.511 cm^2, (d): [Ni(II)] = 0.0627 mol l^{-1} and A = 1.02 cm^2.

formed on the surface of the electrode can affect the shape of the voltammograms The mechanisms for the crystallization of metal on the substrate can be explained by the Volmer-Weber (VW) model, Stranski-Krastanov (SK) model, or Frank-van der Merwe (FM) model,[39,40] but these models are not implemented in the software. Though there are deviations in the cathodic peaks, the anodic peaks are well-matched and the equilibrium potential derived from the simulation closely matches the experimental data and previous research. Also, the charge calculated from the CV curve during the cathodic scan showed similar values, which validates the model used in the simulation.

Kinetics and reversibility of Cr(II)/Cr(0), Fe(II)/Fe(0), Co(II)/Co(0), Ni(II)/Ni(0).—The kinetics of electrochemical reactions can be interpreted by comparing the standard rate constants and diffusion coefficients. They respectively represent the electron transfer rates and mass transport rates. For both properties, orders of magnitude are important rather than exact values. Figure 5a shows the standard rate constants we obtained through both correlation and numerical fitting. Scan rates of 0.1, 0.3, and 0.5 V s^{-1} were selected. In general, an increase in the scan rate leads to a large standard rate constant, but the order of the standard rate constants is very similar for the cases of different scan rates. For all reactions, the standard rate constants are about 10^{-3} cm s^{-1} (see Table SII).

The diffusion coefficients of Cr(II), Fe(II), Co(II), and Ni(II) were obtained by using CV, as shown in Figure 5b. CA was also measured to verify the diffusion coefficients of four ionic species (Figure S1). Again, both numerical fitting and correlations were used. All diffusion coefficients of the four ions were on the order of 10^{-5} cm^2 s^{-1}, showing typical values in liquid phases[15,17–20] (see Table SIII). The specific values of diffusion coefficient show large differences depending on different methods, which may be related to the characteristics of different measurements method involving the potential or current[41] and the difference in the active area of the electrode.[42]

A plot of the peak-to-peak potential vs logarithm of the scan rates can be used to determine the reversibility of the redox reactions according to the scan rates. Figure 6 shows that a scan rate in a range of 0.1–0.5 V s^{-1} can be considered a quasi-reversible region. A slight increase of the peak-to-peak potential is for quasi-reversible regions.[15] The same conclusion can be obtained by calculating the reversibility factors, as listed in Table III. The reversibility factor between 15 and 0.001 is for quasi-reversible cases. These conclusions support the experimental correlations used in this study for calculating thermodynamic and kinetic properties.

Spectroscopic behavior of Fe(II), Co(II), Ni(II).—As shown in Figure 7, absorption spectra were obtained for Cr(III), Ni(II), Co(II),

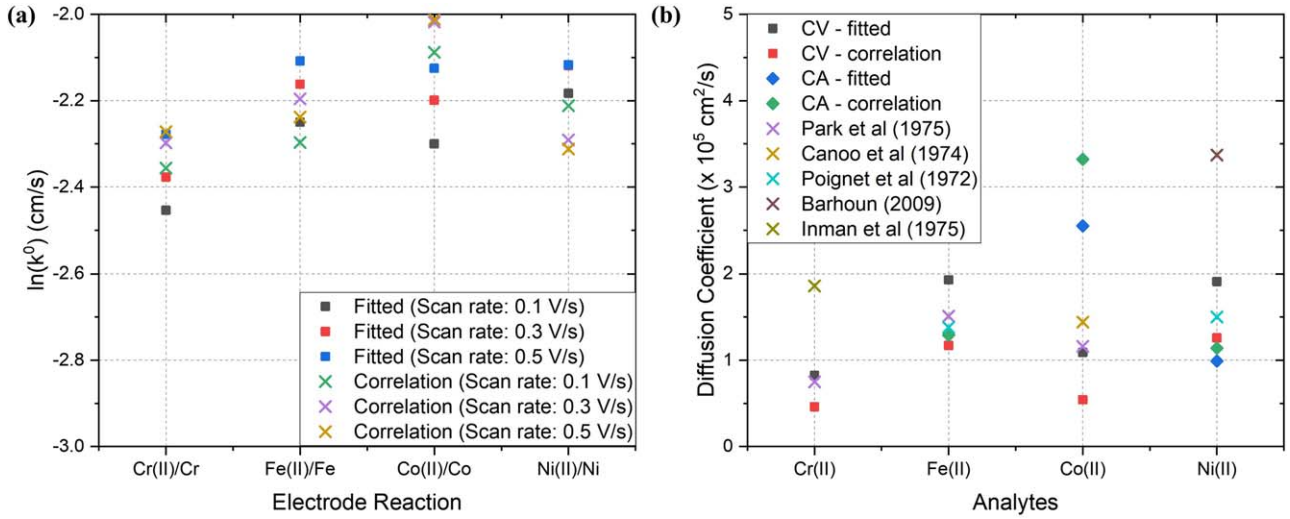

Figure 5. (a) Standard rate constants of four electrode reactions: Cr(II)/Cr(0), Fe(II)/Fe(0), Co(II)/Co(0), Ni(II)/Ni(0), and (b) diffusion coefficients of Cr(II), Fe(II), Co(II), and Ni(II).

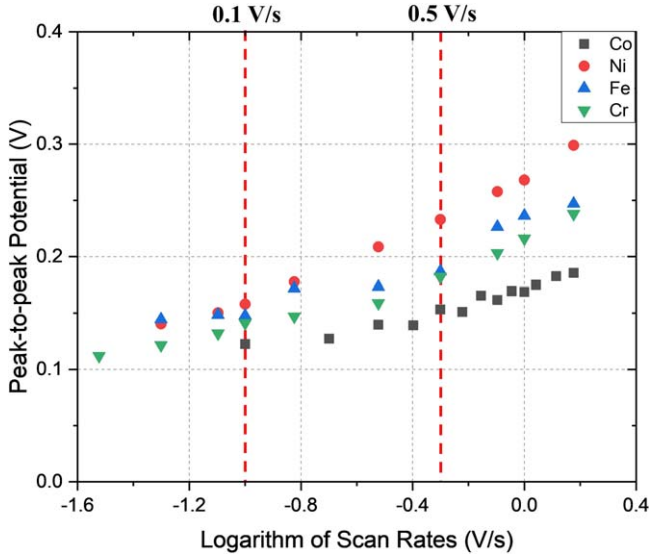

Figure 6. E_{pp} vs scan rate for the four electrode reactions. The peak-to-peak potential increases slightly as the scan rate increases.

and Fe(II) in a Vis-NIR range (400–950 nm) and Fe(II) in a UV range (250–400 nm). Co, Ni, and Cr show d-d transitions in the tested spectral range, while Fe does not. Regarding the selection of measurement ranges, it is known that Fe(II) has no peaks in the visible region, but has peaks in the UV region at 723 K.[43] From our observations, at 773 K, peaks in the UV region no longer appear. This will impede the monitoring of Fe(II) by absorption spectroscopy during electrorefining. On the other hand, Cr(III), Ni(II), and Co(II) show clear peaks in the visible region.

Co shows peaks at 609 nm, 669 nm, and 700.5 nm, which correspond to the $^4A_{2g}(F) \rightarrow {}^4T_{1g}(F)$ transition of the tetrahedral $[CoCl_4]^{2-}$ species. This cobalt species is commonly found in high chloride media. Ni shows a broad, complex peak between 450 and 800 nm composed of multiple absorptions. This is due to the overlap of transitions arising from both tetrahedral and octahedral Ni species, $[NiCl_4]^{2-}$ and $[NiCl_6]^{4-}$, respectively.[44] The two peaks at 628 and 692 nm correspond to the $^3T_{1g}(F) \rightarrow {}^3T_{1g}(P)$ transition of the tetrachloronickelate species. Cr^{3+} has two peaks, arising from the $^4A_{2g}(F) \rightarrow {}^3T_{1g}(P)$ and $^3A_{2g}(F) \rightarrow {}^3T_{1g}(F)$ transitions (549.5 nm and 815 nm, respectively) of the $[CrCl_6]^{3-}$ complex ion.[43]

Table III. Reversibility factors of each electrode reaction at different scan rates. The values show that the electrode reaction is quasi-reversible.

Electrode Reaction	Data type	Reversibility parameter		
		0.1 V s^{-1}	0.3 V s^{-1}	0.5 V s^{-1}
	Reversible region: $\Lambda = 15$			
Cr(II)/Cr	Fitted	0.985	0.694	0.677
	Correlation	1.68	1.11	0.908
Fe(II)/Fe	Fitted	1.03	0.747	0.651
	Correlation	1.2	0.877	0.617
Co(II)/Co	Fitted	1.16	0.928	0.861
	Correlation	2.86	1.95	1.52
Ni(II)/Ni	Fitted	1.24	0.822	0.627
	Correlation	1.41	0.679	0.497
	Irreversible region: $\Lambda = 0.001$			

The molar absorption coefficients were calculated using the Beer–Lambert law:

$$A = \varepsilon LC \quad [12]$$

where A is the absorbance, ε is the molar absorption coefficient, L is the path length, and C is the molarity of the species. Table IV shows the molar absorption coefficients of Ni(II), Co(II), and Cr(III) for the corresponding peaks. The linear regression results of the molar absorption coefficients have an R^2 of over 0.999 for Co(II), 0.001–0.004 mol l^{-1}, and Ni(II), 0.002–0.02 mol l^{-1}, as well as over 0.996 for Cr(III), 0.005–0.03 mol l^{-1}.

Spectroelectrochemical behavior of Cr(III)/Cr(II).— Spectroelectrohemical measurements were applied to observe the Cr (III)/Cr(II) electrode reaction and derive basic properties such as formal potential, number of electrons, and diffusion coefficient of Cr(II). The spectra of Cr(III) and Cr(II) are different. In the case of Cr(II), it is known that it has a peak at slightly over 1000 nm, which is beyond the measured regions.[44] A peak of Cr(III) at 549.5 nm was adopted for comparing the reactions between Cr(III) and Cr(II) since the peak at 815 nm is likely to be overlapped with Cr(II) peaks.

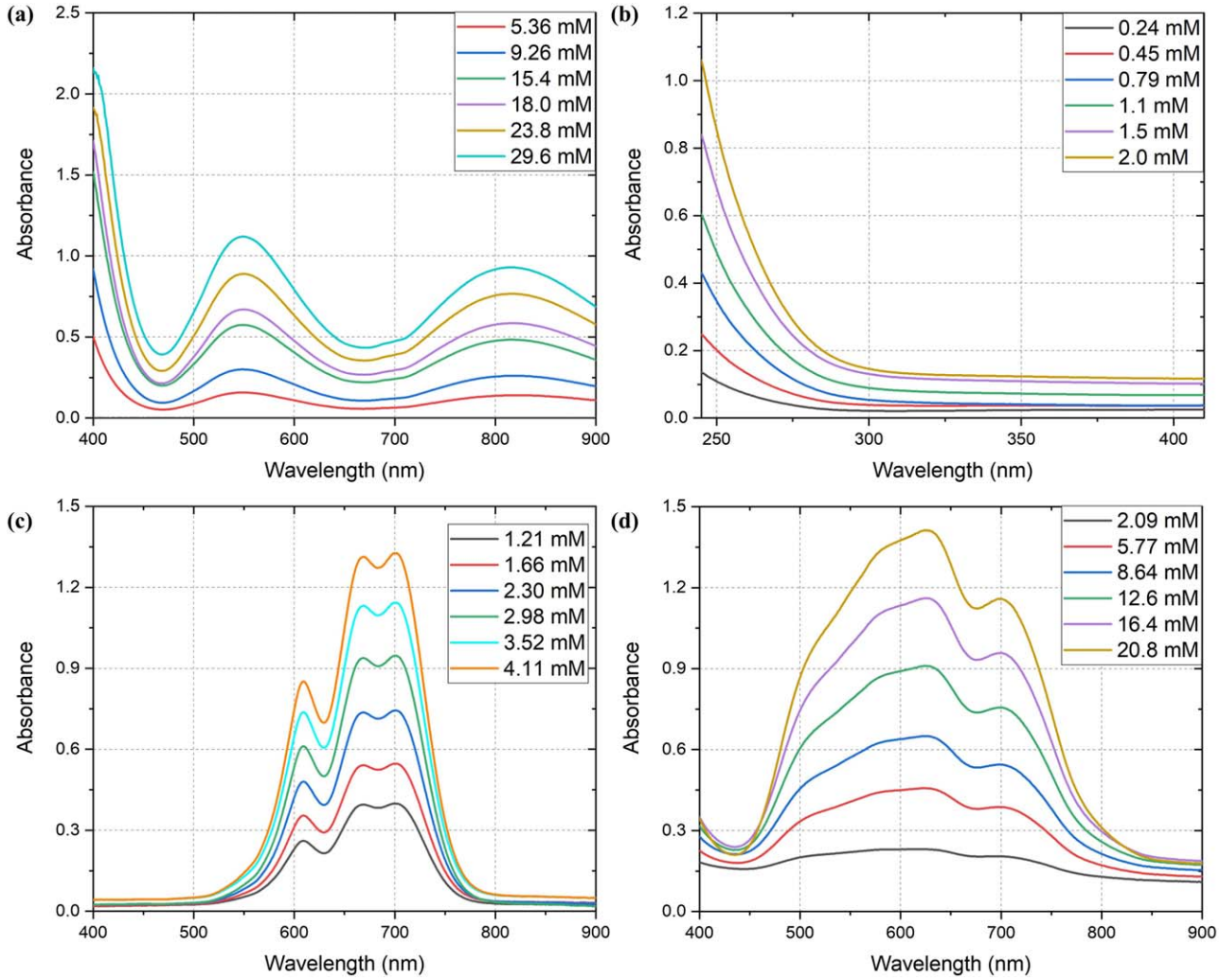

Figure 7. Electronic absorption spectrum of (a) Cr(III), (b) Fe(II), (c) Co(II), and (d) Ni(II).

Table IV. The molar absorption coefficient of Cr(III), Co(II), and Ni(II).

	Cr(III)		Co(II)			Ni(II)	
Wavelength (nm)	549.5	815	609	669	700.5	628	692
Molar absorption coefficient (L/mol/cm)	39.9	33.2	204	317	320	63.8	51.5

Cyclic voltammograms of Cr(III)/Cr(II) are plotted in Figure 8 to determine the applied potential for the spectroelectrochemical measurements. The scan range is $-0.1 \sim 0.9$ V vs Ag^+/Ag. The formal potential for the electrode reaction is estimated by averaging the cathodic peak potential and the anodic peak potential, which is common for soluble-soluble redox pairs.[45] The formal potential is calculated as 0.431 V vs Ag^+/Ag.

From this voltammogram, the potentials of 0.65, 0.55, 0.45, 0.35, 0.25, and 0.15 V vs Ag^+/Ag have been selected. At each potential value, chronoabsorptometry was performed for 40 min, and saturated spectrums were achieved. The spectrums at each potential value were used to fit the Nernst equation, and the chronoabsorptometry result at 0.65 V vs Ag+/Ag was also used for determining the diffusion coefficient of Cr(II). The initial composition of LiCl-KCl-$CrCl_3$ (0.15 wt%) was utilized for spectroelectrochemical measurements.

Since we controlled the electrode potential, the reduction of Cr(II) to Cr(0) can be ignored. Owing to this assumption, the change of Cr(III) concentrations will directly change the concentrations of Cr(II). From the chronoabsorptometry at 0.65 V vs Ag^+/Ag, diffusion coefficients of Cr(II) can be derived. The UV/Vis spectrum was collected while this potential was applied, allowing for the diffusion coefficient to be calculated using the following equation:[46]

$$A = \frac{2\varepsilon_o D_r^{0.5} C t^{0.5}}{\pi^{0.5}} \quad [13]$$

where A is the absorbance, ε_o is the molar absorption coefficient of the oxidized species, D_r is the diffusion coefficient of the reduced species, C is the molar concentration of Cr, and t is time. The diffusion coefficient calculated from this data is $1.15 * 10^{-5}$ cm^2 s^{-1}, which agrees with the data presented in Figure 5b.

Spontaneous reduction of Cr(III) to Cr(II) was observed when a W electrode was inserted into the electrochemical cell containing Cr(III) only. An increase of Cr(II) peaks and a decrease of Cr(III) peaks were simultaneously observed. Also, the color of the solution changes from dark purple to light blue, which is the characteristic color of anhydrous Cr^{2+}. For this reason, it is necessary to perform electrochemical measurements of the Cr(III)/Cr(II) reaction while

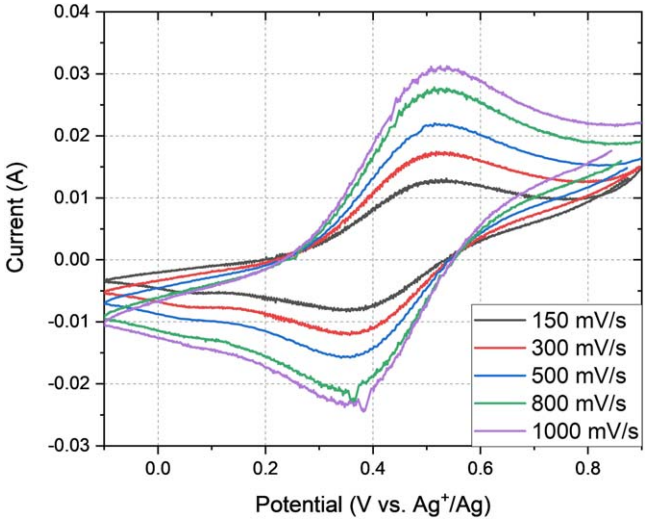

Figure 8. Cyclic voltammograms of Cr(III)/Cr(II) electrode reactions. The formal potential from these voltammograms was measured as 0.431 V vs Ag^+/Ag. [Cr] = 0.0683 mol l^{-1} and A = 1.06 cm^2.

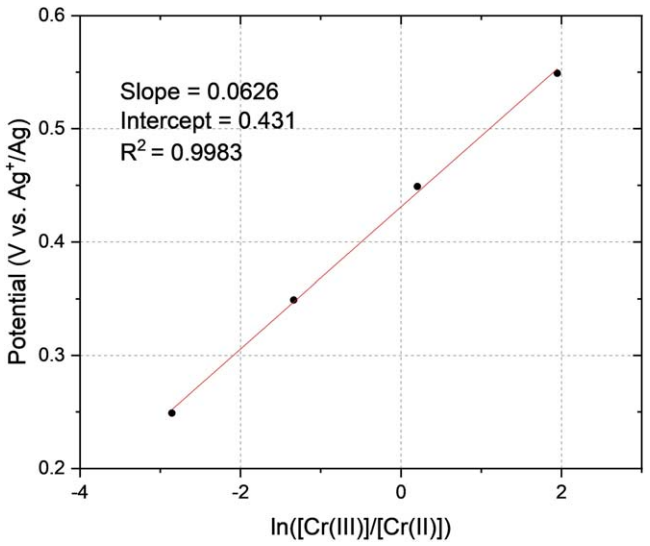

Figure 9. Potential vs concentration ratio of Cr(III) and Cr(II) plot from spectroelectrochemistry.

monitoring the relative concentrations of Cr's two oxidation states. Once the concentrations of Cr(III) and Cr(II) were estimated by the absorption spectrum, they were fitted into the Nernst equation. The following correlations[46] were adopted to estimate the concentration ratio of Cr(III) and Cr(II):

$$E_{app} = E^{f}_{0,Cr(III)/Cr(II)} + \frac{RT}{nF}\ln\left(\frac{[Cr(III)]}{[Cr(II)]}\right) \quad [14]$$

$$\frac{[Cr(III)]}{[Cr(II)]} = \frac{A_{ox} - A}{A - A_{red}} \quad [15]$$

where E_{app} is the applied potential, [Cr(III)] is the molar concentration of Cr(III), [Cr(II)] is the molar concentration of Cr(II), A_{ox} is the absorbance at the potential where the Cr(III) is dominant (0.65 V vs Ag^+/Ag), A is the absorbance at the applied potential, and A_{red} is the absorbance at the potential where Cr(II) is dominant (0.15 V vs Ag^+/Ag).

As shown in Figure 9, the logarithm ratio of concentrations of the two ions shows a linear correlation between the applied potential and

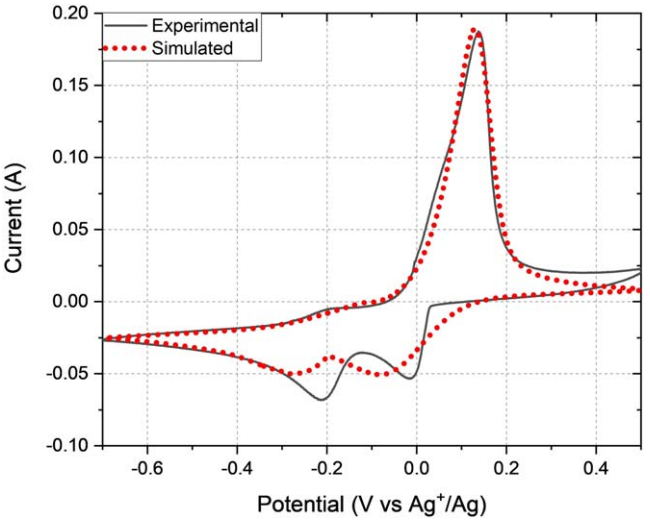

Figure 10. Experimental and simulated cyclic voltammograms of $CoCl_2$-$NiCl_2$-LiCl-KCl at 773 K. [Co(II)] = 0.0610 mol l^{-1}, [Ni(II)] = 0.0627 mol l^{-1}, and A = 0.982 cm^2.

the estimated concentration ratio, which confirms that Cr(III)/Cr(II) follows the Nernstian relationship and the spectroelectrochemical observations are successfully performed. The n value of this electrode reaction derived from the slope of the linear regression is 1.06, which is close to the theoretical value of 1. The formal potential of the reaction is estimated as 0.437 V vs Ag^+/Ag, which agrees with the formal potential derived from Figure 9.

ECE Reaction in a Binary System of Ni and Co.—Combined chemical and electrochemical reactions become important in a multi-component environment. The possible reactions in a binary mixture of Ni(II) and Co(II) were investigated using CV. Figure 10 shows the decrease of the Co oxidation peak at about −0.2 V vs Ag^+/Ag. The reduction peak of the same Co pair was maintained. This phenomenon is ascribed to reduced Co metal reacting with Ni ion and converting to Co ion.[21] This chemical reaction is thermodynamically spontaneous ($\Delta G = -4.516$ kcal).[21]

$$\text{Reduction reaction 1: } Ni^{2+} + 2e^- \rightleftarrows Ni \quad [16]$$

$$\text{Reduction reaction 2: } Co^{2+} + 2e^- \rightleftarrows Co \quad [17]$$

$$\text{Oxidation reaction 1: } Co \rightleftarrows Co^{2+} + 2e^- \quad [18]$$

$$\text{Chemical reaction: } Ni^{2+} + Co \rightleftarrows Co^{2+} + Ni \quad [19]$$

$$\text{Oxidation reaction 2: } Ni \rightleftarrows Ni^{2+} + 2e^- \quad [20]$$

To confirm this hypothesis, the experimental results were compared to the simulation results. For simulations, the formal potentials, diffusion coefficients, and standard rate constants obtained from the numerical fitting method in this study were used. As shown in Fig. 10, the consideration of the spontaneous chemical reaction successfully reproduces the experimental observation of the reduction of Co oxidation peak only. Deviations of the reduction peak occur since the numerical modeling does not consider the nucleation and growth model during the electrodeposition of Co and Ni.[40]

Conclusions

This study has combined electrochemical measurements, UV–vis-NIR absorption spectroscopic observations, and numerical modeling to lay the foundation for developing a new decontamination

process for radioactive metallic wastes. The common alloying components (i.e., Fe, Ni, Cr) and impurity (i.e., Co) of structural components in nuclear power plants are investigated. By applying constant electrode potentials, we successfully conducted spectroelectrochemical investigations of Cr(III)/Cr(II) by comparing the applied potential to the calculated potential from the Nernst equation with spectroscopically determined concentrations. Since this study obtained standard rate constants and diffusion coefficients simultaneously, the quasi-reversibility of redox reactions in the electrochemical systems was thoroughly confirmed according to the scan rates of CV. The obtained reaction properties were used in the numerical modeling of CE reaction mechanisms to reproduce the experimental results of CV in a Ni and Co binary system. The findings of this study will be directly used for producing acceptable waste forms of a final repository. In addition, the decontamination process will reduce the volume of intermediate-level waste by converting a considerable amount of volume to low-level waste and very low-level waste.

Acknowledgments

This work was supported by the Korea Hydro & Nuclear Power Co., Ltd (grant number: 2018-Tech15). It was also supported by the National Research Foundation of Korea, the Ministry of Science and ICT (grant number: 2019M2A7A1001758).

ORCID

Sungyeol Choi https://orcid.org/0000-0002-7164-8491

References

1. D. Robertson, C. Thomas, S. Pratt, E. Lepel, and V. Thomas, *Low-Level Radioactive Waste Classification, Characterization, and Assessment: Waste Streams and Neutron-Activated Metals*, PNNL (2000).
2. Z. Dlouhy, A. Crégut, M. Genova, M. Cross, D. Reisenweaver, M. Laraia, M. Cross, Y. Sivintsev, and R. Smith, *Radiological Characterization of Shut Down Nuclear Reactors for Decommissioning Purposes*, IAEA (1998).
3. W. I. Ko, H. H. Lee, S. Choi, S.-K. Kim, B. H. Park, H. J. Lee, I. T. Kim, and H. S. Lee, *Nucl. Eng. Des.*, **277**, 212 (2014).
4. H. S. Jung, S. Choi, I. S. Hwang, and M.-J. Song, *Prog. Nucl. Energy*, **58**, 27 (2012).
5. J. Park, S. Choi, S. Sohn, K. R. Kim, and I. S. Hwang, *J. Electrochem. Soc.*, **161**, H97 (2014).
6. J. J. Laidler, J. Battles, W. Miller, J. Ackerman, and E. Carls, *Prog. Nucl. Energy*, **31**, 131 (1997).
7. T. Inoue and L. Koch, *Nuclear Engineering and Technology*, **40**, 183 (2008).
8. H. Lee, G. I. Park, K. H. Kang, J. M. Hur, J. G. Kim, D. H. Ahn, Y. Z. Cho, and E. H. Kim, *Nuclear Engineering and Technology*, **43**, 317 (2011).
9. M. Williamson and J. Willit, *Nuclear Engineering and Technology*, **43**, 329 (2011).
10. S. Choi, J. Park, R. O. Hoover, S. Phongikaroon, M. F. Simpson, K.-R. Kim, and I. S. Hwang, *J. Nucl. Mater.*, **416**, 318 (2011).
11. S. Choi, J. Park, K.-R. Kim, H. Jung, I. Hwang, B. Park, K. Yi, H.-S. Lee, D. Ahn, and S. Paek, *J. Alloy. Compd.*, **503**, 177 (2010).
12. T. Koyama, M. Iizuka, Y. Shoji, R. Fujita, H. Tanaka, T. Kobayashi, and M. Tokiwai, *J. Nucl. Sci. Technol.*, **34**, 384 (1997).
13. S. Herrmann and S. Li, *Nucl. Technol.*, **171**, 247 (2010).
14. S. Seo, S. Choi, and B. G. Park, *J. Nucl. Mater.*, **491**, 115 (2017).
15. J. Park, S. Choi, S. Sohn, and I. S. Hwang, *J. Electrochem. Soc.*, **164**, D744 (2017).
16. M. Iizuka, K. Uozumi, T. Inoue, T. Iwai, O. Shirai, and Y. Arai, *J. Nucl. Mater.*, **299**, 32 (2001).
17. C. Canoo and P. Claes, *Electrochim. Acta*, **19**, 37 (1974).
18. J. C. Poignet and M. J. Barbier, *Electrochim. Acta*, **17**, 1227 (1972).
19. H. El Ghallali, H. Groult, A. Barhoun, K. Draoui, D. Krulic, and F. Lantelme, *Electrochim. Acta*, **54**, 3152 (2009).
20. D. Inman, J. C. L. Legey, and R. Spencer, *J. Electroanal. Chem. Interfacial Electrochem.*, **61**, 289 (1975).
21. W.-S. Choi, S.-H. Cho, Y.-J. Lee, Y.-S. Kim, and J.-H. Lee, *J. Electroanal. Chem.*, **866**, 114175 (2020).
22. C. A. Schroll, S. Chatterjee, T. Levitskaia, W. R. Heineman, and S. A. Bryan, *Electroanalysis*, **28**, 2158 (2016).
23. T. J. Kim, B. O. Jeong, E. H. Lee, D. H. Ahn, Y. Jung, and S. W. Paek, *Int. J. Electrochem. Sci.*, **7**, 11257 (2012).
24. H. Lambert, *Molten salt spectroscopy and electrochemistry for spent nuclear fuel treatment*, The University of Manchester (2017).
25. S. Yoon, D. Kang, S. Sohn, J. Park, M. Lee, and S. Choi, *Journal of Nuclear Fuel Cycle and Waste Technology*, **18**, 143 (2020).
26. M. Rudolph, *J. Comput. Chem.*, **26**, 1193 (2005).
27. D. J. Schiffrin, *J. Electroanal. Chem. Interfacial Electrochem.*, **201**, 199 (1986).
28. H. Laitinen and C. Liu, *JACS*, **80**, 1015 (1958).
29. L. Yang and R. G. Hudson, *J. Electrochem. Soc.*, **106**, 986 (1959).
30. D. Yoon, A. Baggett, S. Phongikaroon, J. A. King, and K. Marsden, *J. Electrochem. Soc.*, **166**, E159 (2019).
31. O. Shirai, T. Nagai, A. Uehara, and H. Yamana, *J. Alloy. Compd.*, **456**, 498 (2008).
32. I. Barin, *Thermochemical Data of Pure Substances* (VCH, Germany) (1989).
33. M. Zhang, J. Ge, J. Zhang, and L. E. Liu, *Electrochem. Commun.*, **105**, 106498 (2019).
34. T. Berzins and P. Delahay, *JACS*, **75**, 555 (1953).
35. A. J. Bard and L. R. Faulkner, *Electrochemical Methods*, **2**, 580 (2001).
36. R. S. Nicholson and I. Shain, *Anal. Chem.*, **36**, 706 (1964).
37. H. Matsuda and Y. Ayabe, *Zeitschrift für Elektrochemie, Berichte der Bunsengesellschaft für physikalische Chemie*, **59**, 494 (1955).
38. R. G. Compton and C. E. Banks, *Understanding Voltammetry* (World Scientific, Singapore) (2018).
39. C. P. Fabian, V. Luca, P. Chamelot, L. Massot, C. Caravaca, and G. R. Lumpkin, *J. Electrochem. Soc.*, **159**, F63 (2012).
40. E. B. Budevski, G. T. Staikov, and W. J. Lorenz, *Electrochemical Phase Formation and Growth: An Introduction to the Initial Stages of Metal Deposition* (Wiley, New York) (2008).
41. D. Yoon and S. Phongikaroon, *J. Electrochem. Soc.*, **164**, E217 (2017).
42. G. J. Janz and N. P. Bansal, *J. Phys. Chem. Ref. Data*, **11**, 505 (1982).
43. G. Harrington and B. R. Sundheim, *Annals of the New York Academy of Sciences (U.S.)*, **28**, 950 (1960).
44. G. P. Smith, *Review of Electronic Absorption Spectra of Molten Salts ORNL-3411*, US Atomic Energy Commission (1963).
45. N. Elgrishi, K. J. Rountree, B. D. McCarthy, E. S. Rountree, T. T. Eisenhart, and J. L. Dempsey, *J. Chem. Educ.*, **95**, 197 (2018).
46. D. J. Chesney, *Laboratory Techniques in Electroanalytical Chemistry* (ACS Publications, New York) (1996).